Article

Oxygen Self-Doping in Hollandite-Type Vanadium Oxyhydroxide Nanorods

Igor Djerdj, Denis Sheptyakov, Fabia Gozzo, Denis Arc#on, Reinhard Nesper, and Markus Niederberger

J. Am. Chem. Soc., **2008**, 130 (34), 11364-11375 • DOI: 10.1021/ja801813a • Publication Date (Web): 01 August 2008

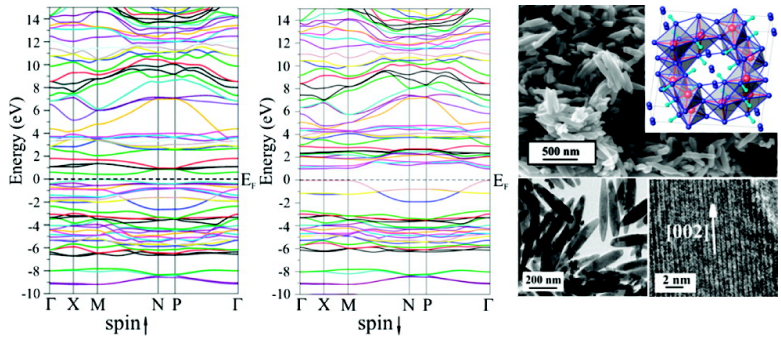

More About This Article

Additional resources and features associated with this article are available within the HTML version:

- Supporting Information
- Links to the 1 articles that cite this article, as of the time of this article download
- Access to high resolution figures
- Links to articles and content related to this article
- Copyright permission to reproduce figures and/or text from this article

View the Full Text HTML

J|A|C|S
ARTICLES

Published on Web 08/01/2008

Oxygen Self-Doping in Hollandite-Type Vanadium Oxyhydroxide Nanorods

Igor Djerdj,[†] Denis Sheptyakov,[§] Fabia Gozzo,[||] Denis Arčon,[⊥,#] Reinhard Nesper,[‡,▽] and Markus Niederberger*[,†]

Department of Materials and Department of Chemistry and Applied Biosciences, ETH Zürich, Wolfgang-Pauli-Strasse 10, 8093 Zürich, Switzerland, Laboratory for Neutron Scattering, ETH Zürich and Paul Scherrer Institute, 5232 Villigen, Switzerland, Swiss Light Source, Paul Scherrer Institute, 5232 Villigen, Switzerland, Institute Jožef Stefan, Jamova 39, 1000 Ljubljana, Slovenia, Faculty of Mathematics and Physics, University of Ljubljana, Jadranska 19, 1000 Ljubljana, Slovenia, and Collegium Helveticum, Common Institution of ETH Zürich and University of Zürich, ETH Zentrum, 8092 Zürich, Switzerland

Received March 14, 2008; E-mail: markus.niederberger@mat.ethz.ch

Abstract: A nonaqueous liquid-phase route involving the reaction of vanadium oxychloride with benzyl alcohol leads to the formation of single-crystalline and semiconducting $VO_{1.52}(OH)_{0.77}$ nanorods with an ellipsoidal morphology, up to 500 nm in length and typically about 100 nm in diameter. Composition, structure, and morphology were thoroughly analyzed by neutron and synchrotron powder X-ray diffraction as well as by different electron microscopy techniques (SEM, (HR)TEM, EDX, and SAED). The data obtained point to a hollandite-type structure which, unlike other vanadates, contains oxide ions in the channels along the *c*-axis, with hydrogen atoms attached to the edge-sharing oxygen atoms, forming OH groups. According to structural probes and magnetic measurements (1.94 μ_B/V), the formal valence of vanadium is +3.81 (V^{4+}/V^{3+} atomic ratio $\approx$ 4). The experimentally determined density of 3.53(5) g/cm^3 is in good agreement with the proposed structure and nonstoichiometry. The temperature-dependent DC electrical conductivity exhibits Arrhenius-type behavior with a band gap of 0.64 eV. The semiconducting behavior is interpreted in terms of electron hopping between vanadium cations of different valence states (small polaron model). *Ab initio* density-functional calculations with a local spin density approximation including orbital potential (LSDA + *U* with an effective *U* value of 4 eV) have been employed to extract the electronic structure. These calculations propose, on the one hand, that the electronic conductivity is based on electron hopping between neighboring V^{3+} and V^{4+} sites, and, on the other hand, that the oxide ions in the channels act as electron donors, increasing the fraction of V^{3+} cations, and thus leading to self-doping. Experimental and simulated electron energy-loss spectroscopy data confirm both the presence of V^{4+} and the validity of the density-of-states calculation. Temperature-dependent magnetic susceptibility measurements indicate strongly frustrated antiferromagnetic interactions between the vanadium ions. A model involving the charge order of the V^{3+} sites is proposed to account for the observed formation of the magnetic moment below 25 K.

Introduction

Anisotropic nanoparticles such as nanotubes, nanorods, and nanowires are of not only scientific but also technological interest. The anisotropy inherent in these nanomaterials provides unique properties which are expected to be critical to the function and integration of nanoscale devices.[1,2] The attractiveness of one-dimensional nanomaterials is also reflected in the large and rapidly growing number of publications in this exciting research field. The interested reader is referred to several excellent review articles.[2–6]

Among the different families of functional materials, metal oxides play an outstanding role due to their redox activity.[7,8] The possibility to change the oxidation state and the stoichiometry provides unique opportunities to tailor the chemical and physical properties. A particularly fascinating example along these lines is the class of anisotropic vanadium oxides with diverse morphologies including nanotubes,[9–11] nanorods,[12–14]

[†] Department of Materials, ETH Zürich.
[§] Laboratory for Neutron Scattering, ETH Zürich and Paul Scherrer Institute.
[||] Swiss Light Source, Paul Scherrer Institute.
[⊥] Institute Jožef Stefan.
[#] University of Ljubljana.
[‡] Department of Chemistry and Applied Biosciences, ETH Zürich.
[▽] Collegium Helveticum.

(1) Hu, J. T.; Odom, T. W.; Lieber, C. M. *Acc. Chem. Res.* **1999**, *32*, 435.
(2) Patzke, G. R.; Krumeich, F.; Nesper, R. *Angew. Chem., Int. Ed.* **2002**, *41*, 2446.
(3) Xia, Y. N.; Yang, P. D.; Sun, Y. G.; Wu, Y. Y.; Mayers, B.; Gates, B.; Yin, Y. D.; Kim, F.; Yan, Y. Q. *Adv. Mater.* **2003**, *15*, 353.
(4) Rao, C. N. R.; Deepak, F. L.; Gundiah, G.; Govindaraj, A. *Prog. Solid State Chem.* **2003**, *31*, 5.
(5) Rao, C. N. R.; Nath, M. *Dalton Trans.* **2003**, 1.
(6) Tang, Z.; Kotov, N. A. *Adv. Mater.* **2005**, *17*, 951.
(7) Rao, C. N. R. *Annu. Rev. Phys. Chem.* **1989**, *40*, 291.
(8) Rao, C. N. R.; Raveau, B. *Transition metal oxides*; VCH Publishers, Inc.: New York, 1995.
(9) Spahr, M. E.; Bitterli, P.; Nesper, R.; Muller, M.; Krumeich, F.; Nissen, H. U. *Angew. Chem., Int. Ed.* **1998**, *37*, 1263.

 10.1021/ja801813a CCC: $40.75

nanowires,[15–18] nanofibers,[19] and nanobelts.[20,21] On the nanoscale dimension, the higher specific surface area emerges as an important improvement compared to bulk systems, having significant implications with respect to energy storage devices,[22–25] sensing,[26] and catalytically active sites.[27–29]

Vanadium oxides are known to exhibit an exceptionally rich variety of structural motifs and electronic ground states.[30–32] Approximately 60 types of vanadium oxide frameworks are divided into five classes based on the type of coordination polyhedra present: tetrahedron, trigonal bipyramid, square pyramid, regular octahedron, and distorted octahedron. V−O compounds can further be divided into 14 subclasses characterized by more complex structural units.[31] Vanadium oxides frequently form low-dimensional structures, where mixed valency of vanadium ions and interplay between spin-charge-orbital degrees of freedom can lead to strongly correlated electronic states. Metal−insulator transitions,[33–35] superconductivity,[36] or unusual spin states can be found.[37] An important and widely investigated class of such low-dimensional structures is represented by the hollandite-type vanadium oxides with the general formula $A_xV_8O_{16}$, where A is an alkaline, alkaline-earth, or another metal cation. The vanadium hollandite structure is, in general, built of zigzag chains formed by edge-sharing VO_6 octahedra. The individual chains are then connected via shared corner oxygen atoms. Zigzag chains are well-known systems where magnetic frustration plays a very important role. Their ground state has been extensively studied in the past as a function of the ratio between the exchange coupling constants J_2/J_1.[38–42] A quantum phase transition from the spin liquid phase to the gapped dimer phase occurs at $J_2/J_1 = 0.2411$.[43] Several different hollandite vanadium oxides with different ions intercalated into the channels are known in the literature,[33–35,44] but only $Bi_xV_8O_{16}$ ($1.6 < x < 1.8$) has been studied in detail due to the observed metal−insulator transition.[33–35] In that particular system, the molar ratio of V^{3+} and V^{4+} is close to 2:1, and it is believed that the charge order, which is proposed to be. . . $V^{3+}V^{3+}V^{4+}$. . . , is a direct consequence of this specific molar ratio.[35] A mechanism in which charge and orbital ordering are cooperative and cause the metal−insulator transition in this system has been proposed.[33] Before now, there is only one report in the literature about a hollandite-type vanadium oxide which contains only anions in the 2×2 tunnels.[45] It has an occupational disorder at the vanadium sites as well as in the tunnels, and it is believed that the vanadium is in the single oxidation state V^{3+}. Concerning magnetic properties, $V_{7.22}O_8(OH)_8Cl_{0.77}(H_3O)_{2.34}$ shows significant spin frustration.[45]

In this work, we present the characterization of a novel hollandite-type compound with the formula $VO_{1.52}(OH)_{0.77}$, containing oxide ions in the 2×2 tunnels. The synthesis is based on a simple one-batch process involving the reaction of vanadium oxytrichloride with benzyl alcohol,[46] analogous to many other nonaqueous liquid-phase processes that use benzyl alcohol as solvent and oxygen-supplying agent.[47,48] In addition to the crystal structure of this compound, which was solved and refined by means of neutron diffraction and synchrotron powder X-ray diffraction (XRD), also its electronic structure was calculated using the local spin density approximation including orbital potential (LSDA + U) method. On the basis of these calculations, electron hopping from neighboring V^{3+} and V^{4+} atoms is proposed as a model for the electronic conductivity. Furthermore, the role of the oxide ions in the channel can be described as an electron donor, resulting in so-called self-doping of this hollandite-type structure. The good agreement of experimentally recorded and theoretically simulated electron energy-loss spectra confirmed the validity of the density of states (DOS) calculation. Morphological features, DC electrical conductivity, and DC and AC magnetic susceptibilities

(10) Krumeich, F.; Muhr, H. J.; Niederberger, M.; Bieri, F.; Schnyder, B.; Nesper, R. *J. Am. Chem. Soc.* **1999**, *121*, 8324.
(11) Niederberger, M.; Muhr, H. J.; Krumeich, F.; Bieri, F.; Günther, D.; Nesper, R. *Chem. Mater.* **2000**, *12*, 1995.
(12) Satishkumar, B. C.; Govindaraj, A.; Nath, M.; Rao, C. N. R. *J. Mater. Chem.* **2000**, *10*, 2115.
(13) Pinna, N.; Wild, U.; Urban, J.; Schlögl, R. *Adv. Mater.* **2003**, *15*, 329.
(14) Pinna, N.; Willinger, M.; Weiss, K.; Urban, J.; Schlögl, R. *Nano Lett.* **2003**, *3*, 1131.
(15) Muster, J.; Kim, G. T.; Krstic, V.; Park, J. G.; Park, Y. W.; Roth, S.; Burghard, M. *Adv. Mater.* **2000**, *12*, 420.
(16) Guiton, B. S.; Gu, Q.; Prieto, A. L.; Gudiksen, M. S.; Park, H. *J. Am. Chem. Soc.* **2005**, *127*, 498.
(17) Wei, M. D.; Sugihara, H.; Honma, I.; Ichihara, M.; Zhou, H. S. *Adv. Mater.* **2005**, *17*, 2964.
(18) Zhou, F.; Zhao, X. M.; Yuan, C. G.; Li, L.; Xu, H. *Chem. Lett.* **2007**, *36*, 310.
(19) Gu, G.; Schmid, M.; Chiu, P. W.; Minett, A.; Fraysse, J.; Kim, G. T.; Roth, S.; Kozlov, M.; Munoz, E.; Baughman, R. H. *Nat. Mater.* **2003**, *2*, 316.
(20) Liu, J. F.; Li, Q. H.; Wang, T. H.; Yu, D. P.; Li, Y. D. *Angew. Chem., Int. Ed.* **2004**, *43*, 5048.
(21) Shi, S. F.; Cao, M. H.; Fle, X. Y.; Xie, H. M. *Cryst. Growth Des.* **2007**, *7*, 1893.
(22) Spahr, M. E.; Stoschitzki-Bitterli, P.; Nesper, R.; Haas, O.; Novak, P. *J. Electrochem. Soc.* **1999**, *146*, 2780.
(23) Wang, Y.; Cao, G. Z. *Chem. Mater.* **2006**, *18*, 2787.
(24) Nordlinder, S.; Nyholm, L.; Gustafsson, T.; Edstrom, K. *Chem. Mater.* **2006**, *18*, 495.
(25) Liu, A. H.; Ichihara, M.; Honma, I.; Zhou, H. S. *Electrochem. Commun.* **2007**, *9*, 1766.
(26) Liu, J. F.; Wang, X.; Peng, Q.; Li, Y. D. *Sens. Actuators, B* **2006**, *115*, 481.
(27) Schlögl, R.; Abd Hamid, S. B. *Angew. Chem., Int. Ed.* **2004**, *43*, 1628.
(28) Guimond, S.; Abu Haija, M.; Kaya, S.; Lu, J.; Weissenrieder, J.; Shaikhutdinov, S.; Kuhlenbeck, H.; Freund, H. J.; Dobler, J.; Sauer, J. *Top. Catal.* **2006**, *38*, 117.
(29) Penner, S.; Klotzer, B.; Jenewein, B. *Phys. Chem. Chem. Phys.* **2007**, *9*, 2428.
(30) Chirayil, T.; Zavalij, P. Y.; Whittingham, M. S. *Chem. Mater.* **1998**, *10*, 2629.
(31) Zavalij, P. Y.; Whittingham, M. S. *Acta. Crystallogr. B* **1999**, *55*, 627.
(32) Livage, J *Coord. Chem. Rev.* **1999**, *190−192*, 391.
(33) Kato, H.; Waki, T.; Kato, M.; Yoshimura, K.; Kosuge, K. *J. Phys. Soc. Jpn.* **2001**, *70*, 325.
(34) Waki, T.; Morimoto, Y.; Kato, H.; Kato, M.; Yoshimura, K. *Phys. B* **2003**, *329−333*, 938.
(35) Waki, T.; Kato, H.; Kato, M.; Yoshimura, K. *J. Phys. Soc. Jpn.* **2004**, *73*, 275.
(36) Yamauchi, T.; Ueda, Y.; Mori, N. *Phys. Rev. Lett.* **2002**, *89*, 057002.
(37) Lumsden, M. D.; Sales, B.; Mandrus, D.; Nagler, S. E.; Thompson, J. R. *Phys. Rev. Lett.* **2001**, *86*, 159.
(38) Eggert, S. *Phys. Rev. B* **1996**, *54*, R9612.
(39) White, S. R.; Affleck, I. *Phys. Rev. B* **1996**, *54*, 9862.
(40) Allen, D.; Senechal, D. *Phys. Rev. B* **1997**, *55*, 299.
(41) Vieira, V. R.; Guihery, N.; Rodriguez, J. P.; Sacramento, P. D. *Phys. Rev. B* **2001**, *63*, 224417.
(42) Maeshima, N.; Hagiwara, M.; Narumi, Y.; Kindo, K.; Kobayashi, T. C.; Okunishi, K. *J. Phys.: Condens. Matter* **2003**, *15*, 3607.
(43) Okamoto, K.; Nomura, K. *Phys. Lett. A* **1992**, *169*, 433.
(44) Kanke, Y.; Takayama-Muromachi, E.; K. K.; Kosuda, K. *J. Solid State Chem.* **1995**, *115*, 88.
(45) Chernova, N. A.; Katana Ngala, J.; Zavalij, P. Y.; Whittingham, M. S. *Phys. Rev. B* **2007**, *75*, 014402.
(46) Niederberger, M.; Bartl, M. H.; Stucky, G. D. *J. Am. Chem. Soc.* **2002**, *124*, 13642.
(47) Niederberger, M.; Garnweitner, G. *Chem. Eur. J.* **2006**, *12*, 7282.
(48) Niederberger, M. *Acc. Chem. Res.* **2007**, *40*, 793.

are also thoroughly studied to obtain a clear picture of the investigated material.

Experimental Section

Materials. Vanadium(V) oxychloride (99.995%) and benzyl alcohol (99.8%, anhydrous) were obtained from Aldrich and used without further purification. The heat treatment was performed in Parr acid digestion bombs with 45 mL Teflon cups.

Synthesis. In a typical synthesis, 0.5 mL (0.92 g; 5.31 mmol) of vanadium(V) oxychloride was slowly added to 20 mL of benzyl alcohol. The vial was sealed and stirred at room temperature for several minutes. The solution color gradually turned from red to green-blue. The reaction solution was then transferred to the autoclave and heated at 150 °C for 24 h in a regular laboratory furnace. The resulting black suspension was centrifuged, and the precipitate was thoroughly washed with ethanol (3 times) and dried at 60 °C in air. The product was finally ground in a mortar to yield a black powder.

Characterization. The XRD pattern was recorded in reflection mode using a Philips PW 3040/60 X'Pert PRO (Almelo, Netherlands) diffractometer with Cu Kα radiation at 45 kV and 40 mA. The step size was set to 0.02° with measuring time of 20 s/step, which is suitable for the Rietveld refinement. The synchrotron powder XRD experiment ($\lambda \approx 0.512$ Å) was performed at room temperature with the high-resolution powder diffractometer located at the Materials Sciences beamline at the SLS synchrotron light source[49] (Paul Scherrer Institute, Villigen, Switzerland). The neutron powder diffraction data ($\lambda \approx 1.515$ Å) were collected at room temperature with the high-resolution neutron diffractometer HRPT[50] at the spallation neutron source SINQ of the Paul Scherrer Institute. The synchrotron X-ray data were used to solve the main structural motif in the space group *I*4/*m* by the software FOX.[51] The neutron data enabled the location of the hydrogen atoms in the structure also by FOX.[51] The final combined refinement of the synchrotron X-ray and neutron powder diffraction data was performed by the software FULLPROF.[52] The microstructural parameters were extracted from the synchrotron XRD powder pattern using the Rietveld method. The profile function was chosen to be the modified Thompson−Cox−Hastings pseudo-Voigt (TCH pV) method, making the size−strain analysis straightforward.[53] In this approach, we assumed that the line-broadening of the deconvoluted profile occurred due to the small crystallite size and the presence of lattice microstrain. The values of half-width parameters *V*, *W*, and *X* were kept constant at instrumental values determined by using the standard sample $Na_2Al_2Ca_3F_{14}$ (cubic system, space group $I2_13$, $a = 10.249$ Å). The highly crystalline anisotropy was modeled assuming a needle-like crystal shape offered within FULLPROF, i.e., considering less broadening in the direction along the needle axis. Scanning electron microscopy (SEM) characterization was performed by using a Zeiss LEO 1530 microscope operating at 5 kV. Transmission electron microscopy (TEM) measurement was performed on a Zeiss EM 912Ω instrument at an acceleration voltage of 120 kV, while high-resolution transmission electron microscopy (HRTEM) characterization was done using a Philips CM200-FEG microscope (200 kV, $Cs = 1.35$ mm) equipped with a GIF 100 GATAN energy filter for electron energy-loss spectroscopy (EELS) measurements. The samples for TEM characterization were prepared in such a way that one drop of the dispersion of as-synthesized powder in ethanol was deposited onto a copper grid covered by an amorphous carbon film. The EELS spectra of the samples were recorded at a collection angle of 8 mrad. The energy resolution, which was estimated from the full width at half-maximum of the zero-loss peak, was found to be 1 eV. The recorded core-loss spectra were subjected to deconvolution using the Fourier ratio method with low-loss spectra recorded under equivalent conditions to reduce multiple-loss events. Finally, the background under the edges was subtracted by applying the standard AE^{-r} background model. The density of the powder was determined at 23 °C using an AccuPyc 1330 gas-penetration pycnometer operating with He gas. DC electrical conductivity was measured from the powder sample pressed into a pellet in the temperature range of 305−439 K, employing the van der Pauw four-probe technique. The pelletized sample was pressed against the cooled surface of a closed-cycle He cryostat (Leybold) installed inside an argon-filled glovebox. A Keithley Source Measure Unit 236 was used as a programmable constant current source, and a Keithley Digital Multimeter DMM 2002 was used for measuring the voltage drop across the sample. The magnetization at applied field was measured with a SQUID magnetometer (MPMS 5S, Quantum Design). Zero-field-cooled (ZFC) and field-cooled (FC) runs were performed between room temperature and 2 K in a static magnetic field of 10 kOe. For the magnetization measurements, the samples were loaded into gelatin capsules and the measurements corrected for the diamagnetic contribution of the sample holder. In the temperature-dependent AC susceptibility ($H = 6.5$ Oe) measurements, in-phase χ' and out-of-phase χ'' signals were recorded simultaneously by a two-channel lock-in amplifier operated at a fundamental frequency ν varied between 1 and 10^3 Hz.

Calculation Details. The first-principles calculation was performed by a full-potential (linearized) augmented plane-wave + local orbitals method ((L)APW + lo) based on the density functional theory (DFT) and implemented in WIEN2K code.[54] Because of the failure of the local spin density approximation (LSDA) due to the presence of localized V 3d electrons, a spin-polarized calculation including orbital correction potential (LSDA + *U*) was run, assuming a ferromagnetic approximation for the paramagnetic state, which simplifies the calculation procedure. The LSDA + *U* (SIC) method introduced by Anisimov et al. was employed in the current approach.[55] The calculation was executed under the presumption that the oxide ion O3 occupies the crystallographic site 2a with the atomic coordinates (0, 0, 0) instead of the refined values (0, 0, 0.101) at 4e. Such an approximation is justified by the fact that the (under)occupancy of the O3 site equals 58% [4e × 0.58 ≈ 2a], and in addition, the *z*-coordinate of O3 can be regarded as 0 with an anisotropic thermal parameter. Consequently, the stoichiometry of the compound for which the DFT calculation was done is $VO_{2.25}H$, which is close to the experimentally determined stoichiometry of $VO_{2.29}H_{0.77}$. The calculation was performed with an energy cutoff constant $R_{MT}K_{max} = 3$, where K_{max} is the cutoff for the plane waves and R_{MT} is the smallest of all muffin-tin radii. Muffin-tin sphere boundaries separate an interstitial region from the ion cores, and their radii were chosen as 1.8 au for V, 1.2 au for O, and 0.6 au for H. Since the system contains hydrogen and hence short OH bonds, the usual settings for such systems have been employed. The effective intra-atomic correlation energy U_{eff} is taken to be 4 eV. A total of 143 *k*-points on a shifted mesh in the irreducible part of the Brillouin zone (IBZ) were used for the self-consistent calculations. The calculation was considered to converge when the total charge of the system was stable within 10^{-4} electron charges.

Results and Discussion

The initial and preliminary analysis of the crystal structure of the vanadium oxyhydroxide nanorods involved Rietveld

(49) http://sls.web.psi.ch/view.php/beamlines/ms/index.html.
(50) Fischer, P.; Frey, G.; Koch, M.; Könnecke, M.; Pomjakushin, V.; Schefer, J.; Thut, R.; Schlumpf, N.; Bürge, R.; Greuter, U.; Bondt, S.; Berruer, E. *Phys. B* **2000**, *276*−*278*, 146.
(51) Favre-Nicolin, V.; Cerny, R. *J. Appl. Crystallogr.* **2002**, *35*, 734.
(52) Rodriguez-Carvajal, J. *Phys. B* **1993**, *192*, 55.
(53) Thompson, P.; Cox, D. E.; Hastings, J. B. *J. Appl. Crystallogr.* **1987**, *20*, 79.
(54) Blaha, P.; Schwarz, K.; Madsen, G. K. H.; Kvasnicka, D.; Luitz, J. *WIEN2K, An Augmented Plane Wave + Local Orbitals Program for Calculating Crystal Properties*; Vienna University of Technology: Vienna, Austria, 2001.
(55) Anisimov, V. I.; Solovyev, I. V.; Korotin, M. A.; Czyzyk, M. T.; Sawatzky, G. A. *Phys. Rev. B* **1993**, *48*, 16929.

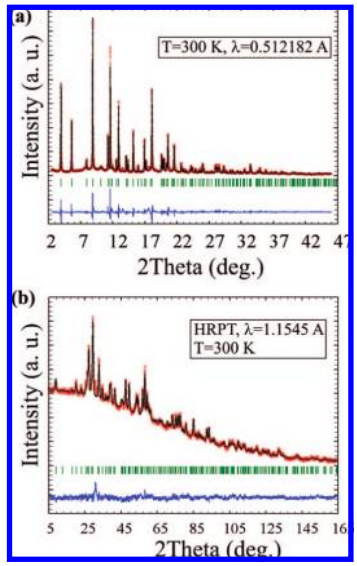

Figure 1. (a) Rietveld plot of the $VO_{1.52}(OH)_{0.77}$ crystal structure refinement from synchrotron X-ray powder diffraction data at room temperature. The measured data points are marked in red, the calculated profile is drawn as a solid black line, and the difference curve is shown in blue. Green bars correspond to the position of the Bragg reflections. (b) Same as in (a) but for the neutron powder diffraction data.

refinement of the X-ray powder diffraction pattern measured by a conventional laboratory XRD machine. The reflections observed matched well with the XRD pattern reported in the ICDD PDF database (No. 00-500-1797), corresponding to $V_{8.18}O_{16}\cdot 1.46\ H_2O$ in the space group $I4/m$. Although the atomic coordinates of this compound were not reported, the space group with the allowed Wyckoff positions for the atoms represented a suitable initial model for further structure solution and refinement. Figure S1 in the Supporting Information presents the Rietveld output plot of the processed XRD powder pattern, indicating a good structural raw model. To get more detailed structural information, including possible hydrogen atoms, high-resolution probes such as synchrotron X-ray and neutron diffraction were performed. The complementarity of X-ray and neutron powder diffraction techniques was essential for the success of the complete crystal structure determination of $VO_{1.52}(OH)_{0.77}$. The scattering amplitudes of vanadium, oxygen, and hydrogen atoms are in the ratio of 23:8:1 for X-rays and roughly −0.4:5.8:−3.7 for neutron diffraction. Consequently, hydrogen is almost invisible by X-rays, whereas vanadium is almost invisible for neutrons. On the other hand, in the neutron diffraction experiment, hydrogen and oxygen atoms strongly scatter. Accordingly, the atomic coordinates of the vanadium atoms are refined on the basis of the synchrotron XRD data and kept constant during the refinement of the neutron diffraction data. Furthermore, they can be well distinguished from each other because the respective neutron scattering lengths are of opposite signs. Figure 1 shows the Rietveld refinement plots of synchrotron X-ray and neutron powder diffraction data, respectively. A significant anisotropic peak-broadening is visible due to the elongated crystal shape of the nanoparticles. The anisotropic peak-broadening is modeled according to the TEM results. The nonspherical shape is also responsible for the imperfections in the fitting procedure, leading to oscillations of the difference curve for the synchrotron data (Figure 1a). The quality of fitting parameters ($R_{wp} = 10.5\%$) is nevertheless satisfactory. The neutron diffraction pattern (Figure 1b) has a substantial background due to the incoherent scattering from hydrogen, thus corroborating its presence in the composition. The two strongest peaks in the otherwise rather flat difference curve correspond to *d*-spacings of 2.169 and 1.672 Å, respectively, and are assigned to traces of an unidentified impurity in such a small quantity that it is not observed in X-ray diffraction. The crystallographic data of the refined structure and selected bond distances are listed in Tables 1 and 2, while the structure is shown in Figure 2, viewed in perspective (a), along the *c*-axis (b), and along the *a*-axis (c). A highly distorted VO_6 octahedron constitutes the basic structural unit building up the vanadium oxide framework.

The symbols of the atoms in Table 2 coincide with the crystallographic site symbols in Table 1. The central vanadium atom is surrounded by three equivalent oxygens atoms, O1 [1.868 (×1) and 1.985 Å (×2) distant], and three equivalent O2 [2.106 (×1) and 2.055 Å (×2) distant]. Due to the high distortion of the VO_6 octahedron, the assignment of the oxygen atoms to apical and equatorial ligands is not completely clear; therefore, we have chosen the shortest (1.868 Å) and the longest (2.106 Å) V−O distances to represent the bond between the central V and the two apical oxygen atoms, although the O1a−V−O2a angle deviates from 180° by about 15°. The remaining four V−O distances in the VO_6 octahedron are then chosen to connect the central V with four equatorial O ligands. The distortion of the VO_6 octahedron is also evident from the deviations of the bond angles from 180° and 90° (Table 2). Such a pronounced distortion removes the triple degeneracy of the t_{2g} orbitals, having strong implications on the electronic structure of this compound (see below). Typical for a hollandite-type structure, the VO_6 octahedra share edges to form double chains parallel to the crystal *c*-axis. Four double chains, rotated roughly by 90° with respect to each other, share corners to form tunnels.

These 2 × 2 tunnels have an approximate diameter (diagonal O−O distance) of 5.477 Å, which is large enough to accommodate large cations or anions. Numerous reports can be found in the literature where metal cations like K, Ti, or even Ba were intercalated into V−O hollandite.[31] Surprisingly, our structure contains oxide ions O^{2-} placed in the center of the channels, which is proven by the same occupancy for the extra oxygen (denoted as O3 and placed in the 4e site) from both synchrotron XRD and neutron diffraction data and additionally confirmed by inspection of the difference Fourier map. Channel oxide ions are frequently reported for ion-conducting apatite-type silicates.[56–59] The oxide anion channel radius, expressed as the distance between the channel oxide anion and the La cation, amounts to 2.271 Å for $La_9SrSi_6O_{26.5}$,[57] 2.288 Å for $La_{9.5}Si_{5.75}Mg_{0.25}O_{26}$,[58] and 2.31 Å for $La_{9.33}Si_6O_{26}$.[56] These channel radii are comparable to the channel size in $VO_{1.52}(OH)_{0.77}$ (either 2.738 Å, half of the oxygen−oxygen distance, or 1.791 Å, half of the H−H distance), implying that the channels in the hollandite structure are large enough for the intercalation of oxide anions. The V−V distance along the chain of VO_6 octahedra is 3.006 Å, while it is 3.293 Å along a double chain. The V−V distance between two different walls is 3.493 Å. Consequently, it is expected that the charge hopping and magnetic exchange will preferentially occur in a direction

(56) Sansom, J. E. H.; Richings, D.; Slater, P. R. *Solid State Ionics* **2001**, *139*, 205.
(57) Beaudet-Savignat, S.; Vincent, A.; Lambert, S.; Gervais, F. *J. Mater. Chem.* **2007**, *17*, 2078.
(58) Kendrick, E.; Sansom, J. E. H.; Tolchard, J. R.; Islam, M. S.; Slater, P. R. *Faraday Discuss.* **2007**, *134*, 181.
(59) Tolchard, J. R.; Slater, P. R.; Islam, M. S. *Adv. Funct. Mater.* **2007**, *17*, 2564.

Table 1. Crystallographic Data and Refined Structural Parameters Obtained from Combined Neutron and Synchrotron X-ray Powder Diffraction

compound name	vanadium oxyhydroxide					
chemical formula	$V_1O_{2.29}H_{0.77}$ or $VO_{1.52}(OH)_{0.77}$					
V-oxidation number	+3.81					
space group	*I*4/*m* (No. 87)					
Z	8					
crystal system	tetragonal					
lattice parameters (Å)	$a = 10.4255(6)$, $c = 3.0056(2)$					
cell volume (Å^3)	326.682(42)					
label	site	*x*	*y*	*z*	site occupancy	$B_{isotropic}$ (Å^2)
V	8h	0.1424(2)	0.6596(2)	0	1	1.18(8)
O1	8h	0.3375(8)	0.9632(6)	0	1	0.99(5)
O2	8h	0.3387(8)	0.7073(6)	0	1	0.99(5)
O3	4e	0	0	0.101(4)	0.58 (1)	0.99(5)
H	8h	0.364(1)	0.401(1)	0	0.77 (1)	0.99(5)
average crystallite size (nm)	49.1					
standard deviation, measure of anisotropy (nm)	3.9					
average crystallite size in [002] direction (nm)	65.4					
average maximum microstrain *e* ($\times 10^{-4}$)	15.5					
R_p, R_{wp} (%)	1.36, 1.80					
goodness of fit (χ^2)	2.3					

Table 2. Calculated Bond Distances and Angles in the VO_6 Coordination Octahedron[a]

bond	multiplicity	value (Å)
V−O1a	×1	1.868
V−O1e	×2	1.985
V−O2a	×1	2.106
V−O2e	×2	2.055
O−H bond length (Å)		0.949
H−H distance within the channel (Å)		3.582

angle	value (deg)
O1a−V−O2a	165.41
O1e−V−O2e	168.21
O1e−V−O1e	98.40
O2e−V−O2e	93.99
O1e−V−O2e (lower)	82.63
O2a−V−O2e	75.37
O2a−V−O1e	92.85
O1a−V−O2e	94.87
O1a−V−O1e	96.66

[a] a, apical; e, equatorial. H-related bond lengths are also listed.

parallel to the crystal *c*-axis. Careful study of the scattering density in the channels revealed that the hydrogen is attached to only one oxygen site, O2. Refinement of the atomic coordinates for H results in a characteristic OH bond length of 0.949 Å. The presence of O3 and H sites and the refinement of atomic occupancies thereof leads to the nonstoichiometric vanadium oxyhydroxide $V_1O_{2.29}H_{0.77}$ [or $VO_{1.52}(OH)_{0.77}$]. To obtain charge neutrality, the formal valence of vanadium is +3.81; i.e., around 80% of vanadium sites are occupied by V^{4+}, and around 20% by V^{3+}. The central channel oxygen O3 looks like it is doubled in Figure 2a. However, such a splitting is, in fact, artificial, since instead of (0, 0, 0.101) for this site, equally good refinement is obtained if O3 is placed in the (0, 0, 0) position and subjected to strong anisotropic thermal motions. The representation of these central oxygens as ellipsoids, which are strongly elongated along the *c*-axis, in fact suggests a very shallow potential for the O3 at the center of the 2 × 2 channel. However, this could also be a split position, in which O3 occupies the upper position in one channel and the lower position in a neighboring channel. To resolve which of these two possibilities is correct (i.e., more stable), DFT calculations were performed in a supercell created from the 1 × 1 × 2 hollandite unit cells. By comparing the total energies of both configurations, we found that the first solution, i.e., O3 placed in the (0, 0, 0) position and subjected to strong anisotropic thermal motions, lies about 26 mRy (0.354 eV) below the energy corresponding to the split position. Although this energy difference is relatively small, we restrict the discussion of the DFT results to the first and more stable configuration. The nearest neighbors of O3 are hydrogen atoms, suggesting that the oxide anions are stabilized by hydrogen bonds.

The morphology of the $VO_{1.52}(OH)_{0.77}$ nanoparticles was examined by SEM and TEM. An overview SEM image at low magnification illustrates that the product is almost exclusively composed of discrete and uniform particles with an anisotropic, rod-like shape (Figure 3a). The pointed ends of the rods give them an ellipsoidal, rice-like appearance, which is also confirmed by the TEM image in Figure 3b. Their length ranges from 140 to 500 nm, with an average of 330 nm, and the width varies between 50 and 105 nm, with an average of 80 nm. The local crystallinity of a single nanorod was further elucidated by HRTEM, revealing well-developed lattice fringes that extend over the whole area displayed in Figure 3c without any defects. The corresponding power spectrum (Figure 3d) was used for the determination of the zone-axis orientation and the growth direction of the nanorods. The lattice plane distances of 5.212 and 2.888 Å are clearly resolved, corresponding to the (020) and (011) planes. In addition, the selected area electron diffraction (SAED) pattern (Figure 3e), taken from just a part of a single nanorod, can be indexed in accordance with the power spectrum. Both reciprocal space patterns point to single-crystallinity of the nanorod. Its orientation with respect to the electron beam is determined as [100], and the growth direction is deduced from the power spectrum as being along [002].

Consequently, the observed anisotropy in the synchrotron as well as in the laboratory XRD patterns is modeled assuming [002] as the preferential growth direction of the nanorods, resulting in slightly higher values for the crystallite size in the [002] direction (65.4 nm) compared to the average value in all directions (49.1 nm). The discrepancy between the average length of the nanorods and the average crystallite size in the [002] direction implies that the nanorods are probably composed of several single-crystalline subunits that are epitaxially arranged

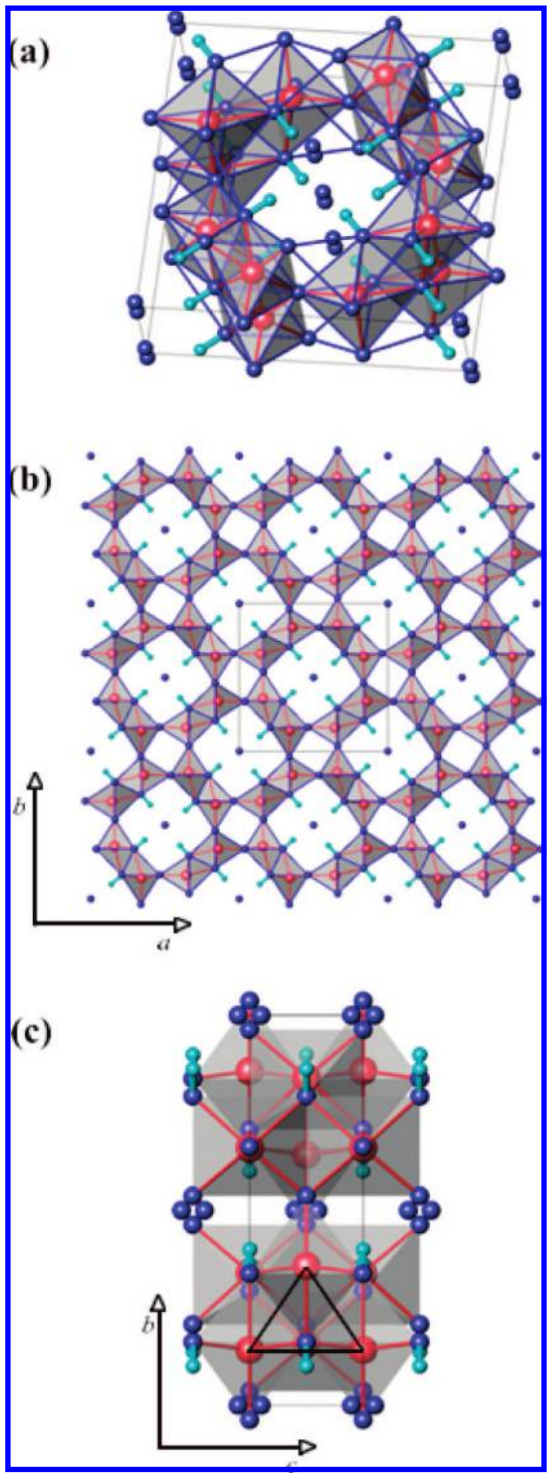

Figure 2. Crystal structure of $VO_{1.52}(OH)_{0.77}$ viewed (a) in perspective, (b) along the *c*-axis, and (c) along the *a*-axis. The vanadium atoms are represented by red, oxygen by blue, and hydrogen by green spheres.

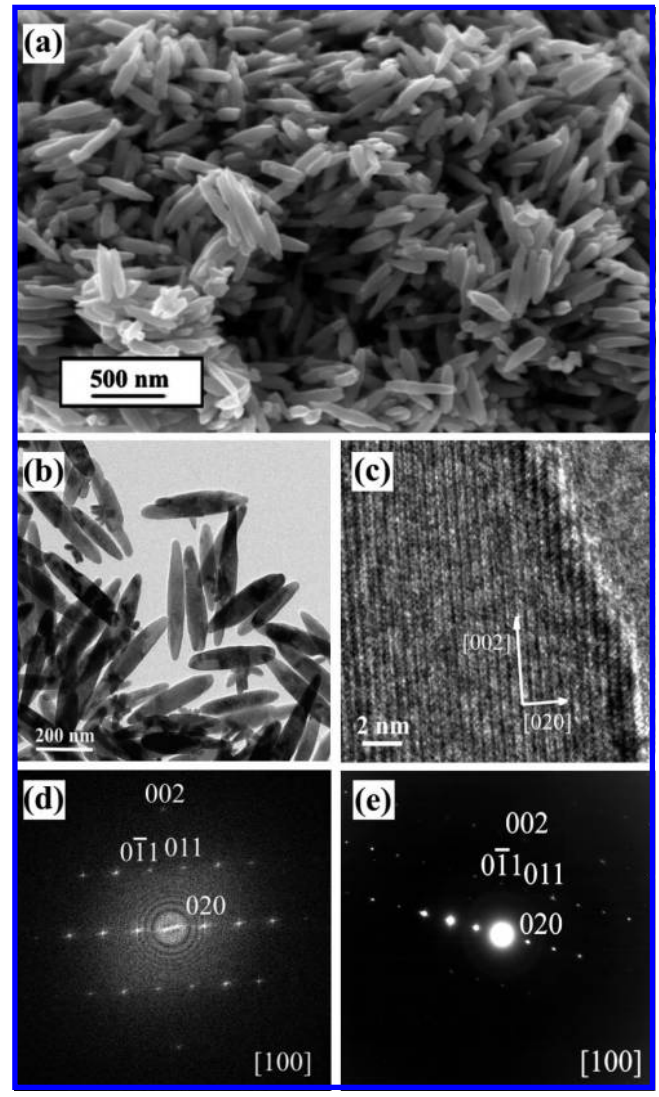

Figure 3. (a) SEM and (b) TEM overview images of $VO_{1.52}(OH)_{0.77}$ nanorods. (c) HRTEM image of a part of a nanorod. (d) Power spectrum corresponding to the images in (c). (e) SAED pattern taken from the part of the nanorod depicted in (c).

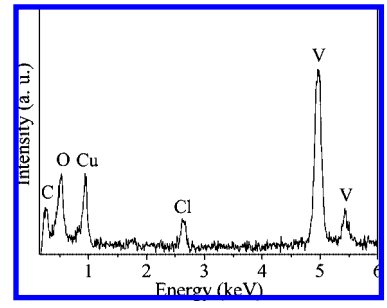

Figure 4. EDX spectrum recorded for the $VO_{1.52}(OH)_{0.77}$ nanorods.

with respect to each other via oriented attachment. In Figure S2 in the Supporting Information, an additional HRTEM image recorded at a different spot is shown to further confirm [002] as the growth axis. Although both HRTEM images (Figure 3c and Figure S2 in the Supporting Information) show a defect-free crystal structure in the area studied, the appreciable microstrain value of 0.15%, deduced from synchrotron XRD, points to the presence of lattice defects. This observation seems to be typical for nanoparticulate systems of reduced dimensionality, like nanorods or nanofibers.[60]

The energy-dispersive X-ray (EDX) spectrum (Figure 4) shows peaks of V, O, and Cl with an atomic ratio of 32.3:62.4:5.3. The other detected elements, Cu and C, originate from the carbon-coated copper grid used for the TEM analysis. The qualitative agreement between the nonstoichiometric formula proposed previously (O/V atomic ratio = 2.29) and the atomic

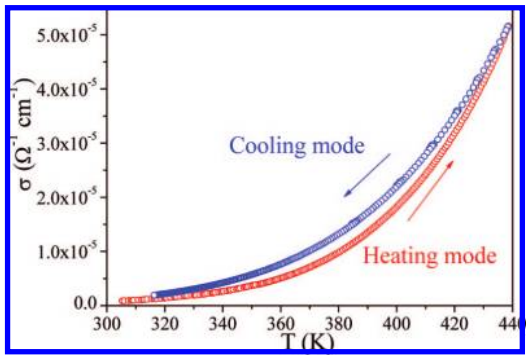

Figure 5. Plot of the DC conductivity of the $VO_{1.52}(OH)_{0.77}$ nanopowder pressed into a pellet.

composition calculated from EDX (O/V atomic ratio = 1.93) is reasonably good, taking into account that EDX is not able to detect hydrogen and that chlorine was not considered in the chemical formula nor in the structural model. Nevertheless, it is present in considerable amount. There are several possibilities to rationalize the presence of chlorine. Either it is accommodated within the channels as a part of the structure, or it is attached to the surface of the nanorods. The third possibility is that the impurity detected by neutron diffraction also contains chlorine. To answer this question, a density measurement was carried out. The resulting density from three measurements is 3.53(5) g/cm^3. Based on the proposed formula of $VO_{1.52}(OH)_{0.77}$ and $Z = 8$, the calculated theoretical density of the material equals 3.59(3) g/cm^3, agreeing quite well with the experimental result. However, we have to point out that Rietveld refinement of the neutron diffraction data can similarly be well fitted to the formula $VO_{1.23}(OH)_{0.77}Cl_{0.18}$; i.e., the oxide ions are replaced by chloride ions. But the theoretical density of such a compound amounts to 3.65(3) g/cm^3, deviating more from the experimental value. These findings suggest that the chlorine detected by EDX is located not within the channels but on the surface of the $VO_{1.52}(OH)_{0.77}$ nanorods and/or in the impurity.

Temperature-dependent measurements of the DC electrical conductivity σ were performed on the powder sample pressed into pellets (Figure 5). The conductivity exhibits typical exponential semiconducting-like behavior in the temperature interval of 305−439 K. The Arrhenius law for thermally activated conduction [$\sigma = \sigma_0 \exp(-E_\sigma/kT)$, where k is the Boltzmann constant, T is the temperature, σ_0 is the pre-exponential factor, and E_σ is the activation energy] is proven by the linear dependence of ln σ on $1/T$. Since the two $\sigma(T)$ curves show a small thermal hysteresis, a least-squares fit was applied separately to each curve (heating, cooling), yielding two activation energies E_σ. Based on the relation $E_g = 2E_\sigma$, where E_g is the band gap energy, we obtain an experimental band gap for the nanorods of 0.64 and 0.76 eV for the cooling and heating cycles, respectively. Due to the experimental setup for conductivity measurement (splitting off of the contacts after cooling), we take the cooling branch as more reliable, and therefore the band gap of 0.64 eV will be considered with higher reliability. The electrical resistivity of the oxide-containing hollandite nanorods at 32 °C was found to be 1.2×10^6 Ω·cm, which is 3 orders of magnitude higher than the corresponding resistivity of its chloride counterpart (2×10^3 Ω·cm).[45] However, one should keep in mind that such a direct comparison is generally inappropriate if the morphological features of the two materials are different. The presence of transition metal ions in the mixed oxidation states (V^{3+} and V^{4+} with the ratio $V^{3+}/(V^{3+} + V^{4+}) = 0.2$) indicates that the electronic properties arise from electron hopping between V^{3+} and V^{4+} ions. They can be described by the small polaron model, in which the conductivity is expressed by a modified Arrhenius formula proposed by Mott.[61] Figure S3 in the Supporting Information shows the DC conductivity in a plot of ln σT vs $1/T$ recalculated from the cooling branch. The dependence is linear, which means that the small polaron model accounts very well for the experimental data in the measured temperature range, and the fit to the Mott formula gives an activation energy for conduction of 0.35 eV.

Because the LSDA method failed to correctly predict the semiconducting ground state as evidenced from the DC conductivity measurement, LSDA + U was applied, assuming that only the 3d states of vanadium exhibit a tendency toward localization, whereas all other electrons are considered as itinerant within the LSDA scheme. The good basis set for the projection of DOS onto the d states in the simulation is obtained with the following choice of the orientation of the local system (x,y,z) at the vanadium site: $(1/\sqrt{2})(\pm1,0,1)$ and (0,1,0) with reference to the a, b, and c directions in the conventional tetragonal cell ($a = b$). With such a choice, the local axes are oriented toward the nearest oxygen sites that build up the VO_6 octahedron in such a way that the z-axis is simultaneously aligned parallel to the shortest (1.868 Å) and the longest V−O bond (2.106 Å), while the x- and y-axes are directed toward the other four previously defined equatorial oxygens. The cubic component of the octahedral crystal field leads to a classic three-below-two crystal field splitting: The five-fold degenerate 3d orbitals split into a higher energy, doubly degenerate e_g level and a lower energy, triply degenerate t_{2g} level. The e_g states comprise the $3d_{z^2}$ and $3d_{x^2-y^2}$ orbitals, whose lobes point toward the octahedral oxygen along the axes of the chosen local coordinate system. In the case of the t_{2g} states, the $3d_{xy}$ orbital points toward the orbital of type similar to that of the second nearest neighbor of the vanadium atom, which is the vanadium atom from the same vertical chain along the c-axis with the lattice vector c (3.006 Å). The $3d_{xz}$ and $3d_{yz}$ orbitals are directed toward the respective orbitals of the vanadium atoms of a double chain 3.293 Å apart. The first Brillouin zone of the primitive body-centered tetragonal lattice used for the calculation of the band structure is displayed in Figure 6a. It encloses a dodecahedron consisting of eight squares and four distorted elongated hexagons. The elongation of the dodecahedron is determined by the tetragonality (c/a), which for this system equals 0.2883. For the band structure calculation, the special k-points of the first Brillouin zone were chosen. The corresponding circuit is denoted in Figure 6a, colored in green, and includes the following special k-points: Γ (0 0 0), the center of the Brillouin zone; X (0 0 1/2) and N (0 1/2 0), the centers of the faces; M (−1/2 1/2 1/2), the center of an edge; and P (1/4 1/4 1/4), a corner point joining three edges. The coordinates in the parentheses express the position of the k-points in units of reciprocal primitive vectors. The band structure of $VO_{1.52}(OH)_{0.77}$, calculated along the selected high-symmetry lines within the first Brillouin zone for a majority spin-up projection and for a minority spin-down projection, is shown in Figure 6b,c, respectively, and it is represented using connected colored lines, where each color indicates one irreducible representation

(60) Djerdj, I.; Garnweitner, G.; Su, D. S.; Niederberger, M. *J. Solid State Chem.* **2007**, *180*, 2154.

(61) Livage, J. *Chem. Mater.* **1991**, *3*, 578.

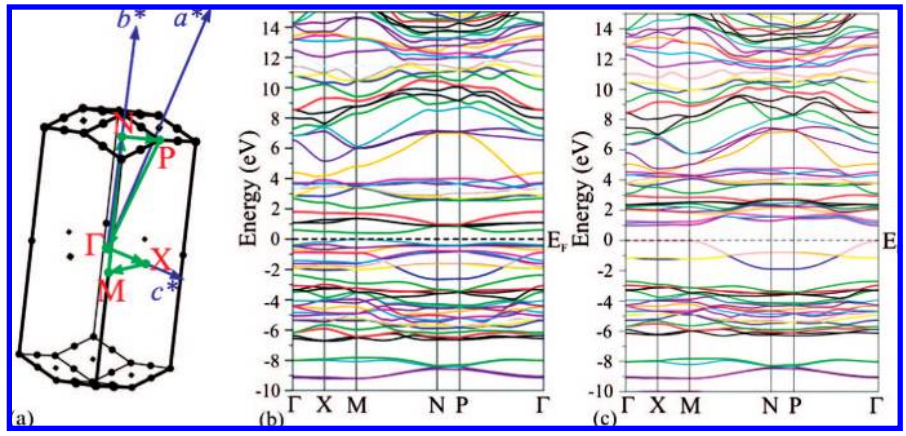

Figure 6. (a) First Brillouin zone of the primitive body-centered tetragonal lattice. The special *k*-points (Γ, X, M, N, P), reciprocal primitive vectors, and the circuit, colored in green, for the calculation of the band structure are denoted. (b) Calculated band structure for spin-up (↑) states of $VO_{1.52}(OH)_{0.77}$ along the high-symmetry lines within the first Brillouin zone. (c) Calculated band structure for spin-down (↓) states. The zero point of the energy is set at the Fermi level.

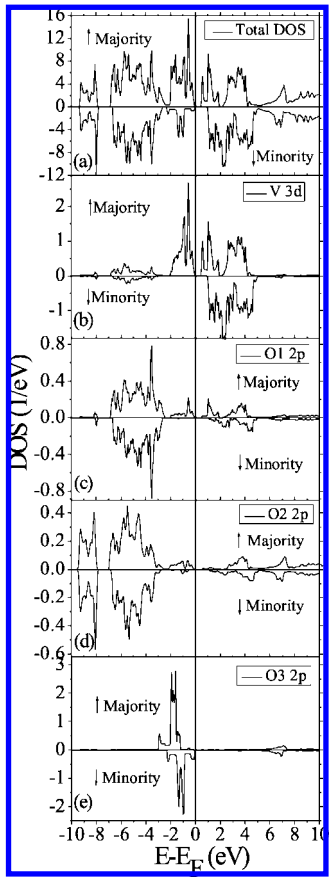

Figure 7. Total DOS of $VO_{1.52}(OH)_{0.77}$ and partial DOS for V, O1, O2, and O3 calculated for both spin channels.

for this symmorphic space group. The calculated total density of states as well as the partial densities of the oxygen 2p and vanadium 3d states are displayed in Figure 7. At low energies, there is a group of bands between −10 and −8 eV corresponding to H 1s states hybridized with O2 2p states, which is clearly visible in Figure 7d. This strong overlap of H 1s and O2 2p orbitals is expected due to the fact that hydrogen is attached to O2 of the VO_6 framework, as experimentally confirmed. The following group of bands from −7 to −2.5 eV is composed of mainly O 2p states, but in this range there is also a non-negligible contribution from the V 3d states. From the molecular-orbital point of view, the bands with mainly O 2p character can be interpreted as the O 2p-dominated lower σ and higher π states. At higher energy, in the spin-up channel between −2.5 and −1.5 eV, there are three bands colored blue, light brown, and yellow that correspond to O 2p states of the oxide ions (denoted also as O3 in Figure 7) in the channels. The same bands in the spin-down channel are shifted toward the Fermi level, forming thus the top of the valence band.

The dispersion of the bands of the oxide ions is large (around 1 eV) along M−N (i.e., parallel to the diagonal of the *ac* plane in the conventional tetragonal lattice) and Γ−P (along a space diagonal), while it is small along Γ−X (i.e., parallel to the diagonal of the *ab* plane) and N−P (along the *b*-axis). Consequently, a geometrical consideration of the band dispersions implies that the 2p electrons of the oxide anions are well localized in the *ab* crystal plane but less localized along the conventional tetragonal *c*-axis. Assuming O3 in the (0 0 0) position, O3−O3 separation measured along the *c*-axis equals 3.0056 Å (lattice parameter *c*). Obviously, the O3−O3 distance along the *c*-axis is short enough to account for such a large band dispersion along the same axis. We also noticed that the O3 spin-up and spin-down bands have different energy positions, providing compelling evidence for the magnetic exchange. The exchange splitting is 0.643 eV, as determined from the shift of the peaks between the majority and minority O3 DOS. Such an exchange may be directly related to our ferromagnetic approximation of the paramagnetic state and may change if other (i.e., antiferromagnetic state) approximations are applied. The group of bands between −2 and 4 eV for the spin-up and between 0 and 5 eV for the spin-down channel corresponds to V 3d states with the admixture of O 2p states, as evidenced from Figure 7. The last group of energy bands, which lies high in energy (higher than 4 eV for ↑ or 5 eV for ↓), belongs to the V 4s,p states.

The angular momentum projected DOS at the vanadium site (Figure 8) shows some interesting features. The minority channel clearly reveals the almost perfect splitting of the 3d t_{2g} and e_g groups of bands due to the cubic component of the octahedral crystal field. The t_{2g} states appear almost exclusively in the energy range from 1 to 3 eV, while the bands between 3 and 5 eV are dominated by the e_g states. The small $t_{2g}-e_g$ configuration mixing is a direct consequence of the octahedral distortion

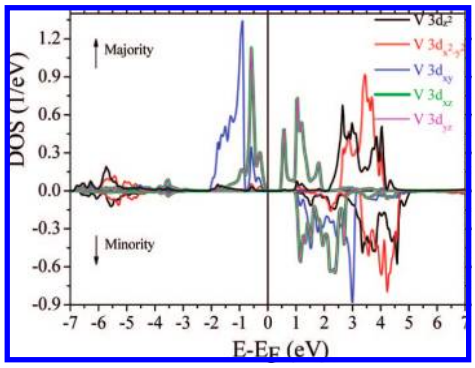

Figure 8. d-Pojected DOS at the V site. The Fermi level E_F is set to 0 eV.

observed in the diffraction experiments. It is noteworthy that the contribution of the e_g states to the admixture of O 2p and V 3d bands in the valence band is higher, forming thus σ bonds, as compared to the contribution of the t_{2g} states, which give rise to π bonds. The respective antibonding π^* and σ^* states are formed in the conduction band by t_{2g} and e_g states hybridized with O 2p states. This observation is in agreement with the choice of the local coordinate system at the V site, with the e_g orbitals pointing toward the six O ligands. However, due to the facts that the vanadium atom is a bit shifted out of the equatorial plane spanned by the four oxygen atoms and that the angle between the apical oxygen−vanadium and opposite apical oxygen atoms deviates from 180°, the contribution of the e_g orbitals reaches into the π^* region (Figure 8). Furthermore, it is interesting to notice that, for the spin-down channel in the region from −2 eV up to the Fermi level, there are bands of exclusively O 2p character without any admixture with V 3d states. They originate from the oxide ions in the channel, O3. The band gap, which amounts to 0.91 eV, is then formed between occupied O3 2p states and empty V 3d (t_{2g}) states. The fact that pure p states extend to the Fermi level means that these states can be used as electron reservoirs, causing a nonintegral population of the d bands. Similar behavior was reported in the case of CrO_2.[62]

Regarding the majority spin bands, one can see in the upper part of Figure 8 that, besides the octahedral crystal field splitting of the V 3d levels similar to that observed in the minority channel, there is a further splitting of the three-fold degenerate t_{2g} orbital into a lower d_{xy} and a higher congruent d_{xz}/d_{yz} orbital. In this case, only the d_{xy} orbital is fully occupied, and the d_{yz}/d_{xz} orbitals are only partially filled due to the fact that some of these bands lie in the valence band and some are positioned in the lower part of the conduction band. This result demonstrates the orbital ordering among the t_{2g} orbitals. Recalling the spatial directionality of d_{xy}, d_{xz}, and d_{yz} orbitals whose lobes point toward the lobes of equivalent orbitals of neighboring metal sites within the double vertical chain along the *c*-axis, one might expect a V−V coupling similar to that in the case of metallic VO_2.[63] According to the strength of the interaction between 3d electrons of neighboring atoms in oxides, they may be either itinerant or localized. Goodenough obtained a semiempirical expression for the room-temperature critical separation of localized vs itinerant 3d electrons in oxides, which is 2.94 Å for a $V^{4+}-V^{4+}$ ion.[64] In our case, the shortest $V^{4+}-V^{4+}$ distances within the same double chain (3.006 and 3.293 Å) are larger than this critical distance, implying that the $3d_{xy}$ and $3d_{xz}/3d_{yz}$ electron orbitals are localized. Among the t_{2g} orbitals, the $3d_{xy}$ electron orbitals lie lowest in energy in the spin-up channel, followed by $3d_{xz}/3d_{yz}$, whose corresponding bands form the top of the valence band together with a minute contribution of the $3d_{xy}$ orbitals, which can be deduced from the overlapped peaks in the corresponding DOS (Figure 8). However, the $3d_{xz}/3d_{yz}$ bands also lie at the bottom of the conduction band, forming thus the band gap of 0.42 eV. This band gap and the band gap in the spin-down channel are obviously direct band gaps, because the maxima of the valence band coincides with the minima of the conduction band at the *M* point of symmetry in reciprocal space. Recalling the finding that the formal valence of vanadium in the $VO_{1.52}(OH)_{0.77}$ is +3.81, around 80% of the vanadium site is occupied by V^{4+} and around 20% by V^{3+}. The vanadium site with V^{4+} contains only one spin-up d-electron in the $3d_{xy}$ orbital, while the V^{3+} sites have a second d-electron in the $3d_{xz}/3d_{yz}$ orbital with the same spin orientation. This information can be extracted from the band structure in the spin-up configuration, where all the bands corresponding to the $3d_{xy}$ states are occupied, while the occupation of the bands with $3d_{xz}/3d_{yz}$ character is proportional to the V^{3+} fraction. This observation elucidates the mechanism of semiconductivity in this compound, obviously involving the hopping of an extra electron to the acceptors of the same tunnel wall. If an extra electron with spin-up configuration is in an initial band corresponding to the $3d_{xz}/3d_{yz}$ state (at V^{3+} site), then it can hop only to the nearest V^{4+} site on the neighboring chain; in terms of energy, it crosses the Fermi level and ends up in the corresponding conduction band. Splitting of the partially filled $3d_{xz}/3d_{yz}$ bands occurred due to orbital polarization induced by the strong on-site Coulomb interactions. Similar to the spin-down channel, the p−d hybridization causes additional O 2p contributions to the 3d group of bands, forming bonding−antibonding σ and π states. The main difference is that the empty $3d_{xz}/3d_{yz}$ states hybridized with O 2p states constitute the antibonding π^* states in the conduction band, while the rest of the $3d_{xz}/3d_{yz}$ states from the valence band form the respective bonding π states. The $3d_{xy}$ states are less hybridized with the O 2p states: their corresponding DOS curves mutually overlap less compared to $3d_{xz}/3d_{yz}$ and O 2p states, leading to a higher localization of the $3d_{xy}$ orbitals.

The LSDA + *U* band calculation with the effective orbital potential value of $U_{eff} = 4$ eV for V 3d electrons yields the semiconducting ground state, in agreement with the experimental data. Such an employed DFT scheme tends to enhance the localization of the t_{2g} electrons and introduces correlation effects of the Mott−Hubbard type. The strongly correlated nature of the $VO_{1.52}(OH)_{0.77}$ system is reflected in the high value of the effective Hubbard *U*, U_{eff}, compared to the bandwidth *W* (∼2 eV), which in fact opens the band gap. Another important and interesting aspect is the contribution of the oxide ions in the channels to the semiconductivity. We showed previously that its pure 2p bands form the top of the valence band in the spin-down channel. These electrons are then released to the conduction band, occupying the empty $3d_{xz}/3d_{yz}$ states and increasing the effective number of the V^{3+} sites that represent the origin of the hopping electrons. Such materials might be considered as located in the negative charge-transfer gap region of the

(62) Korotin, M. A.; Anisimov, V. I.; Khomskii, D. I.; Sawatzky, G. A. *Phys. Rev. Lett.* **1998**, *80*, 4305.
(63) Eyert, V. *Ann. Phys.* **2002**, *11*, 650.
(64) Goodenough, J. B. *J. Solid State Chem.* **1971**, *3*, 490.

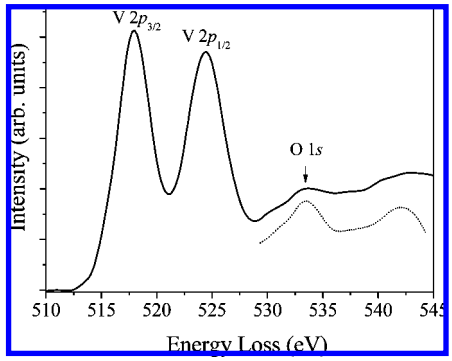

Figure 9. V 2p and O 1s core electron excitation spectrum of $VO_{1.52}(OH)_{0.77}$ after correction for background and multiple scattering. Calculation of the oxygen edge is displayed with the dotted line.

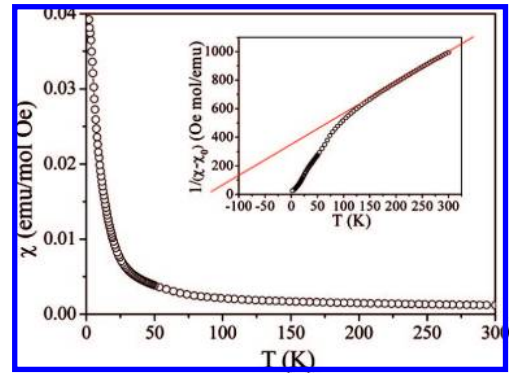

Figure 10. Temperature dependence of the magnetic susceptibility χ measured in DC field $H = 1000$ Oe. The inset shows the reciprocal susceptibility as a function of the temperature. The straight line is the best fit to the Curie−Weiss law at high temperatures (150−300 K).

Zaanen−Sawatzky−Allen diagram,[65] which is not unusual for transition metal oxides containing cations in high oxidation states and with rather high electron affinities. In our case, the contribution of the oxide ions to the band structure in a certain way prefers to allocate the compound in the negative charge-transfer gap region.

To further elucidate the vanadium oxidation state and to study the local electronic structure, we performed an EELS measurement in the core electron excitation region. Figure 9 shows the electron energy-loss spectrum of $VO_{1.52}(OH)_{0.77}$ over an energy range of 510−545 eV. The spectrum can be divided into one region below 528 eV, reflecting the V 2p contribution, and one above 528 eV, assignable to O 1s. The peaks at 518.1 and 524.5 eV correspond to excitations from the V $2p_{3/2}$ (L_3) and V $2p_{1/2}$ (L_2) core levels, respectively. Due to its strong sensitivity to the electronic configuration (the occupation of the d orbital), a reliable indicator for the determination of the oxidation state of the vanadium is the intensity ratio of the V $3p_{3/2}$ to V $3p_{1/2}$ excitations, $I(L_3)/I(L_2)$. Theoretical considerations based on $2j + 1$ degeneracy in a one-electron model gave for L_3/L_2 an intensity ratio of 2:1.[66] However, experimental values for the L_3/L_2 intensity ratio deviate from 2:1 due to a strong interaction between the hole in the V 3p core level and the electron excited into the unoccupied V 3d band from the core level, the so-called core−hole interaction.[67,68]

It was found that, if the oxidation state of vanadium decreases, the L_3/L_2 intensity ratio increases.[69] According to Waddington et al., this ratio for V^{3+} is 1.46 and for V^{5+} it amounts to 0.89.[70] Comparison of the reported EELS spectra for the V−O system indicates that the L_3/L_2 intensity ratio is less than 1 for V_2O_5, close to 1 for VO_2, and more than 1 for V_2O_3.[69,71] In our case, the measured L_3/L_2 intensity ratio in Figure 9 equals 1.09, which is, according to these literature reports, the signature of V^{4+}.

The unoccupied O 2p states are accessible to experimental probes, because they appear as a fine structure (electron energy-loss near-edge structure, ELNES) in the O K ionization edge. In this context, one has to remember that, within a one-electron approximation, the simulation of the L-edge fails due to the strong electron correlation effects.[72] Therefore, we focused on the O K-edge, which is modeled using the simulation module TELNES, combined with the band structure calculations. The experimental O 1s part of the EELS spectrum consists of a single left-hand asymmetric peak centered around 534 eV (denoted by the arrow) and a broad peak around 544 eV. The former is assigned to the transitions from O 1s core level to a final 2p state in σ^* hybridization with a vanadium 3d state, while the latter is attributed to the transition from the O 1s core level to the empty V 4s,4p band. The peak, which appears as a shoulder of the main peak centered at 534 eV, belongs to the transition from the O 1s state to a final 2p state in π^* hybridization with a V 3d state. The simulated O K ELNES fine structure (dotted line in Figure 9) is in good agreement with the experimental data, additionally corroborating the validity of the band structure calculations. The calculated and experimentally observed O K edges show the absence of a clear separation of peaks arising from the transitions from the O 1s state to a final 2p state in π^* and σ^* hybridization with a vanadium 3d state, although in the calculated DOS such a separation is clearly visible. This observation can be explained by the fact that the total calculated O K ELNES is the overall contribution from different non-equivalent oxygen atoms in a specific spin channel. Each contribution has its own individual shape, which is shown in Figure S4 in the Supporting Information. O1 and O2 contribute with exactly the same spectral shape, whereas O3 does not contribute at all due to the absence of final states for the transition. As a result of summing up all the individual contributions, the π^* and σ^* overlap and are not clearly distinguishable in the total experimental and simulated O K edge.

Vanadium oxides often have intriguing magnetic properties, and therefore the temperature dependence of the magnetic susceptibility was measured. DC magnetic susceptibility increases monotonically with decreasing temperature in the range between 300 and 1.5 K (Figure 10). However, its temperature dependence cannot be simulated with a single model over the entire temperature range. A clear demonstration of the complexity of the DC susceptibility temperature dependence is seen from the plots of the inverse magnetic susceptibility χ^{-1} (inset to

(65) Zaanen, J.; Sawatzky, G. A.; Allen, J. W. *Phys. Rev. Lett.* **1985**, *55*, 418.
(66) Sparrow, T. G.; Williams, B. G.; Rao, C. N. R.; Thomas, J. M. *Chem. Phys. Lett.* **1984**, *108*, 547.
(67) Abe, H.; Terauchi, M.; Tanaka, M.; Shin, S.; Ueda, Y *Jpn. J. Appl. Phys* **1997**, *36*, 165.
(68) Abe, H.; Terauchi, M.; Tanaka, M.; Shin, S *Jpn. J. Appl. Phys* **1998**, *37*, 584.
(69) Lin, X. W.; Wang, Y. Y.; Dravid, V. P.; M, M. P.; Kung, M. C. *Phys. Rev. B* **1993**, *47*, 3477.
(70) Waddington, W. G.; Rez, P.; Grant, I. P.; Humphreys, C. J. *Phys. Rev. B* **1986**, *34*, 1467.
(71) Gloter, A.; Serin, V.; Turquat, C.; Cesari, C.; Leroux, C.; Nihoul, G. *Eur. Phys. J. B* **2001**, *22*, 179.
(72) Willinger, M.; Pinna, N.; Su, D. S.; Schlögl, R. *Phys. Rev. B* **2004**, *69*, 155114.

Figure 10) and the χT (Figure S5 in the Supporting Information). Two possible magnetic transitions are indicated: (i) the first transition at around 80 K, where χ^{-1} starts to deviate from the linear dependence and χT slightly increases, showing thermal hysteresis, and (ii) the second transition below 20 K, where χT rapidly drops to zero.

Let us first try to analyze the high-temperature range between 300 and ~80 K. Since the magnetic susceptibility at high temperatures does not converge to zero, we assume that the measured χ has two contributions in this range: a Curie−Weiss contribution, $\chi_{CW} = C/(T - \theta)$, due to the localized vanadium moments, and the temperature-independent contribution, χ_0. The latter contribution is due to the diamagnetic term, χ_{dia}, and the orbital Van-Vleck paramagnetism, χ_{VV}; i.e., $\chi_0 = \chi_{dia} + \chi_{VV}$. Alternatively, χ_0 could arise also from the temperature-independent Pauli paramagnetism of itinerant electrons, but this possibility has been already ruled out on the basis of conductivity measurements. To estimate χ_{dia}, we use Pascal constants and derive -20.6×10^{-6} emu mol^{-1} Oe^{-1} for $VO_{1.52}(OH)_{0.77}$. To reliably estimate χ_{VV}, however, one needs to measure the magnetic susceptibility at very high temperatures, much higher than the temperature set by the exchange interaction. Literature values for χ_{VV} of other known vanadium oxides (including hollandites) are typically around $(1-2) \times 10^{-4}$ emu mol^{-1} Oe^{-1}. Since χ_0 is rather ill defined, this makes the fitting very unstable, and the extracted parameters strongly depend on the choice of temperature interval. If one attempts to fit the susceptibility data between 300 and 150 K with $\chi(T) = \chi_{CW} + \chi_0$ and taking $\chi_0 = 2 \times 10^{-4}$ emu mol^{-1} Oe^{-1} from other systems, then the obtained parameters are $C = 0.457(2)$ emu mol^{-1} Oe^{-1}, $\theta = -157(2)$ K. The deviation from the fit below ~150 K, which is clearly revealed in the inverse susceptibility plot after χ_0 subtraction (inset in Figure 10), could arise from the short-range order effects discussed below. However, it is very easy to understand the obtained Curie constant. The Curie constant $C = 0.457(2)$ emu mol^{-1} Oe^{-1} corresponds to $p_{eff} = 1.91\ \mu_B$. For V^{4+} and V^{3+}, one can calculate the expected effective moments to be 1.73 and 2.83 μ_B, respectively. The average effective moment for 81% V^{4+} and 19% V^{3+} is thus $(0.81 \times 1.73 + 0.19 \times 2.83)\mu_B = 1.94\ \mu_B$, which is very close to what we find from our fits.

The $\chi-T$ plot also suggests an additional anomaly at very low temperatures, i.e., below 20 K (Figure S6 in Supporting Information), where the measurements taken during the ZFC and FC runs differ. Although charge disorder on vanadium may suggest some kind of a spin-glass ground state, we note that the shape of the FC and ZFC curves is not typical for spin-glasses, where a kink in the magnetic susceptibility is expected. It rather resembles a weak ferromagnetic or even superparamagnetic state. To distinguish weak ferromagnetism from superparamagnetism, AC susceptibility measurements were performed. Figure 11 shows the temperature dependence of the real part of the AC susceptibility (χ') at different frequencies between 1 Hz and 1 kHz. We find that χ' increases rapidly at the temperature at which DC χ measured under ZFC−FC conditions starts to differentiate. Although the change in the measurement frequency affects the values of χ', there is no clear shift of the transition temperature, $T_C \approx 25$ K, and only a small reduction of $\chi'(T)$ for $T < T_C$ is observed with increasing frequency. The imaginary part of the AC susceptibility, $\chi''(T)$, shows a steep rise at T_C and a clear maximum well below T_C at $T' = 11$ K ($\nu = 1$ Hz), as shown in the inset of Figure 11. T' is only weakly frequency-dependent and increases to $T' = 12.1$ K for $\nu = 100$ Hz. The appearance of the frequency-dependent maximum in $\chi''(T)$ below T_C suggests dynamic spin freezing for temperatures $T' < T_C$. The absence of a corresponding feature in $\chi'(T)$ can be understood as a consequence of the large real part of the susceptibility associated with a weak ferromagnetic ground state.

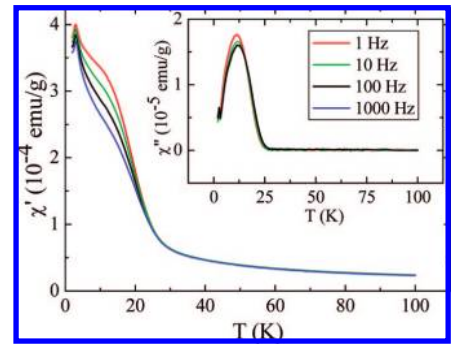

Figure 11. Temperature dependences of real, χ', and imaginary, χ'' (inset), components of AC susceptibility measured with AC field of amplitude $H = 6.5$ Oe at various frequencies.

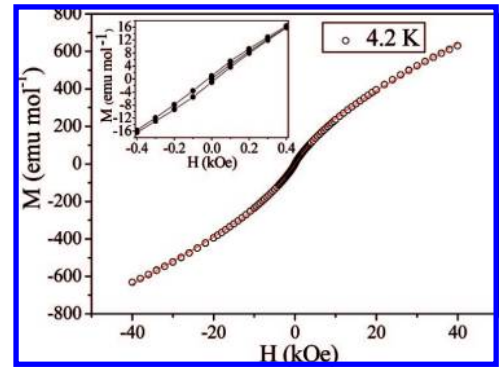

Figure 12. Magnetization curve taken at $T = 4.2$ K. Inset: Enlarged view of the magnetic hysteresis curve up to $H = 400$ Oe.

The magnetization curve (Figure 12) taken at $T = 4.2$ K strongly speaks for the formation of a magnetic moment below ~25 K. The hysteresis is superimposed on the linear-field-independent contribution, χ_{lin}, which may originate from the orbital part described above. The $M(H)$ curve (apart from the hysteresis effect) can be well described as a sum of two contributions:

$$M(H) = \chi_{lin} H + ng\mu_B J B_J\left(\frac{g\mu_B H}{k_B T}\right) \quad (1)$$

Here, J is the total angular momentum and B_J is the Brillouin function standing for the description of the magnetic part. The fit of experimental data to the function $M(H)$ given by eq 1 is also displayed in Figure 12. We find a fairly large χ_{lin} contribution, i.e., $\chi_{lin} = 11.8 \times 10^{-3}$ emu mol^{-1} Oe^{-1}, suggesting that, in the low-temperature phase, the orbital contribution is very important. The total angular momentum is found to be $J = 8.5$, which is consistent with the formation of magnetic clusters.

In order to understand the low-temperature magnetic properties, we recall that the Curie−Weiss temperature is $\theta = -157(2)$ K and then compare this value with the transition temperature $T_C = 25$ K. The ratio between these two temperatures is $\theta/T_C = 6.3$. This ratio is taken as an empirical measure of frustra-

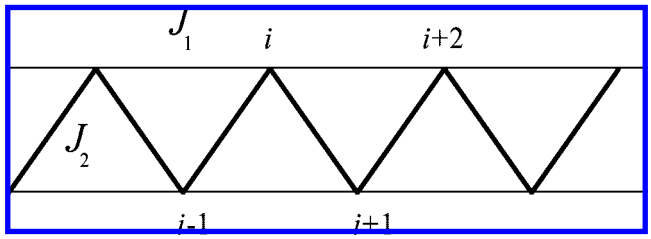

Figure 13. Zigzag chain of vanadium ions in the hollandite structure.

tion,[73] and the materials with θ/T_C close to or larger than 10 are considered strongly frustrated materials. The presence of frustration and a quasi-one-dimensional magnetic structure are likely responsible for the short-range order effects and also explain the deviations of the magnetic susceptibility from the Curie−Weiss law up to ~150 K. The occurrence of frustration in hollandite structures may not be so unexpected from the structural point of view. The channel walls are built of double chains of edge-sharing VO_6 octahedra, where the overlap of t_{2g} orbitals leads to strong exchange antiferromagnetic coupling. On the other hand, the exchange coupling between the neighboring walls is predicted to be small, judging from the V−O−V angle. The arrangement of the vanadium ions in the individual channel wall can be mapped on the so-called zigzag chain (Figure 13). This system has been extensively studied in the past. Two different ground states, a spin-liquid ground-state and a gapped dimer phase, were found depending on the ratio between the exchange coupling constants along the chain and perpendicular to the chain. In our case, the V^{4+} ($S = {}^1/_2$) zigzag chain is interrupted with the V^{3+} ($S = 1$) moments, which act as magnetic impurities. We suggest that, at very low temperatures, these moments locally polarize their neighborhood either via weak interchain coupling or via second nearest-neighbor interactions, leading to a local staggered magnetization within a region characterized by a correlation length ξ. At very low temperatures, ξ increases sufficiently to account for the magnetic ordering. This order should not be taken independently from the suggested orbital ordering. The system we report in this work has a molar ratio of $V^{4+}/V^{3+} = 4{:}1$. If our hypothesis of orbital and charge order is correct, then the low-temperature charge order should be. . . $(V^{4+}V^{4+})(V^{4+}V^{4+})V^{3+}$. . . , where within each $(V^{4+}V^{4+})$ pair their $S = {}^1/_2$ spins pair into singlet state. The remaining V^{3+} ($S = 1$) moments contribute to the observed Curie−Weiss behavior as well as initiating the low-temperature magnetic ordering.

Conclusions

A simple solvothermal reaction between $VOCl_3$ and benzyl alcohol resulted in the formation of ellipsoidal nanorods with a novel hollandite-type structure with the formula $VO_{1.52}(OH)_{0.77}$. Thorough structural characterization by laboratory powder XRD, synchrotron powder XRD, and neutron diffraction revealed that the crystal structure consists of a framework of highly distorted VO_6 octahedra arranged in double chains along the *c*-axis, resulting in a 2×2 tunnel structure, with oxide ions occupying the centers of these tunnels. Hydrogen atoms are attached to one of the oxygens from the VO_6 octahedra, leading to hydroxyl groups. According to the structural probes as well as the magnetic measurements, the formal valence of vanadium is +3.81. The experimentally evidenced semiconducting properties clearly demonstrated the need for involving *U* together with the spin polarization in the band structure calculations, underlining that, in this nanomaterial, electron correlations play a crucial role. The band structure calculation also suggested a hopping mechanism of the electrons between V^{3+} and V^{4+} neighboring sites. Additionally, the oxide ions in the channels lead to a self-doping effect by acting as an electron donor, increasing the concentration of the V^{3+} cations. The magnetic properties are highly complex, involving antiferromagnetic correlations, frustration effects, and formation of a magneticly ordered state below $T_C = 25$ K.

The $VO_{1.52}(OH)_{0.77}$ nanorods are an instructive example of how a simple, one-pot synthesis procedure can result in the formation of a highly complex material. The application of several state-of-the art characterization tools was required to elucidate the structural and physical properties. Some of the results were rather unexpected, and only the combination of experimental data with theoretical modeling made it possible to understand and interpret them. There is no doubt that, in addition to synthetic work, the detailed investigation of the physical and structural properties is equally important toward a fast implementation of nanomaterials into technological applications.

Acknowledgment. Financial support from ETH Zürich is gratefully acknowledged. We express our gratitude to Prof. Robert Schlögl and Dr. Dang Sheng Su from the Fritz-Haber-Institute in Berlin for the use of the electron microscope. We also thank Flavio Mornaghini for the SEM measurements, Dr. Noemi S. Csaba for the density measurement, Dr. Marc Petitmermet for computer assistance, Dr. Marc Willinger for helpful discussions related to the DFT calculation, Dr. Nenad Tomašić for valuable help regarding the matching of the initial XRD data with ICDD structures, and Christian Mensing for magnetization and conductivity measurements. We are also indebted to Prof. René Monnier, Laboratory for Solid State Physics, ETH Zürich, for fruitful discussions concerning the band structure calculation.

Supporting Information Available: XRD pattern of $VO_{1.52}(OH)_{0.77}$ recorded by a laboratory XRD; HRTEM analysis of $VO_{1.52}(OH)_{0.77}$ nanorod taken at a different spot, additionally evidencing the preferential growth direction [002]; DC conductivity plot expressed as $\ln \sigma T$ against $1/T$; individual contributions of the different oxygen atoms to the O*K* ELNES; temperature dependence of χT; low-temperature ZFC/FC curves measured in magnetic field of 10 Oe. This material is available free of charge via the Internet at http://pubs.acs.org.

JA801813A

(73) Ramirez, A. P. *J. Appl. Phys.* **1991**, *70*, 5952.